

Coexistence of Dirac and Weyl points in non-centrosymmetric semimetal $NbIrTe_4$

Qingxin Liu(刘清馨), Yang Fu(付阳), Pengfei Ding(丁鹏飞), Huan Ma(马欢), Pengjie Guo(郭朋杰), Hechang Lei(雷和畅), and Shancai Wang(王善才)

Citation: Chin. Phys. B, 2024, 33 (**4**): 047104. DOI: 10.1088/1674-1056/ad2a79
Journal homepage: http://cpb.iphy.ac.cn; http://iopscience.iop.org/cpb

What follows is a list of articles you may be interested in

Band structures of strained kagome lattices

Luting Xu(徐露婷) and Fan Yang(杨帆)
Chin. Phys. B, 2024, 33 (**2**): 027101. DOI: 10.1088/1674-1056/ad0291

Robust and intrinsic type-III nodal points in a diamond-like lattice

Qing-Ya Cheng(程青亚), Yue-E Xie(谢月娥), Xiao-Hong Yan(颜晓红), and Yuan-Ping Chen(陈元平)
Chin. Phys. B, 2022, 31 (**11**): 117101. DOI: 10.1088/1674-1056/ac7c00

Mottness, phase string, and high-T_c superconductivity

Jing-Yu Zhao(赵靖宇) and Zheng-Yu Weng(翁征宇)
Chin. Phys. B, 2022, 31 (**8**): 087104. DOI: 10.1088/1674-1056/ac7a14

Electronic structures of vacancies in $Co_3Sn_2S_2$

Yuxiang Gao(高于翔), Xin Jin(金鑫), Yixuan Gao(高艺璇), Yu-Yang Zhang(张余洋), and Shixuan Du(杜世萱)
Chin. Phys. B, 2021, 30 (**7**): 077102. DOI: 10.1088/1674-1056/abfa05

Electronic properties of defects in Weyl semimetal tantalum arsenide

Yan-Long Fu(付艳龙), Chang-Kai Li(李长楷), Zhao-Jun Zhang(张昭军), Hai-Bo Sang(桑海波), Wei Cheng(程伟), Feng-Shou Zhang(张丰收)
Chin. Phys. B, 2018, 27 (**9**): 097101. DOI: 10.1088/1674-1056/27/9/097101

RAPID COMMUNICATION

Coexistence of Dirac and Weyl points in non-centrosymmetric semimetal $NbIrTe_4$

Qingxin Liu(刘清馨)[1,2,†], Yang Fu(付阳)[1,2,†], Pengfei Ding(丁鹏飞)[1,2], Huan Ma(马欢)[1,2], Pengjie Guo(郭朋杰)[1,2,‡], Hechang Lei(雷和畅)[1,2,§], and Shancai Wang(王善才)[1,2,¶]

[1] *Department of Physics, Key Laboratory of Quantum State Construction and Manipulation (Ministry of Education), Renmin University of China, Beijing* 100872, *China*

[2] *Beijing Key Laboratory of Opto-Electronic Functional Materials & Micro-Nano Devices, Renmin University of China, Beijing* 100872, *China*

(Received 25 January 2024; revised manuscript received 18 February 2024; accepted manuscript online 19 February 2024)

Using angle-resolved photoemission spectroscopy and density functional theory calculations methods, we investigate the electronic structures and topological properties of ternary tellurides $NbIrTe_4$, a candidate for type-II Weyl semimetal. We demonstrate the presence of several Fermi arcs connecting their corresponding Weyl points on both termination surfaces of the topological material. Our analysis reveals the existence of Dirac points, in addition to Weyl points, giving both theoretical and experimental evidences of the coexistence of Dirac and Weyl points in a single material. These findings not only confirm $NbIrTe_4$ as a unique topological semimetal but also open avenues for exploring novel electronic devices based on its coexisting Dirac and Weyl fermions.

Keywords: Fermi arc, Weyl point, Dirac point, angle-resolved photoemission spectroscopy

PACS: 71.18.+y, 71.20.–b, 79.60.–i **DOI:** 10.1088/1674-1056/ad2a79

1. Introduction

The discovery of three-dimensional topological semimetals has significantly advanced the theory and classification of quantum materials. Dirac and Weyl semimetals, characterized by their unique electronic structures, have garnered extensive research interest. These materials exhibit extraordinary physical properties, including an additional π Berry phase, chiral anomaly, extremely large magnetoresistance, and ultra-high carrier mobility, paving the way for the development of low-dissipation electronic devices.[1–4] A defining feature of Dirac and Weyl semimetals is their topologically protected linear band dispersions near the Fermi level (E_F). The intersections of these bands, known as Dirac points (DPs) and Weyl points (WPs), are pivotal in topological phase transitions and are closely associated with the topological invariant.[5,6] In Dirac semimetal, the DPs are protected by certain symmetry, such as C_{4v} symmetry. Breaking certain symmetries can transform a DP into two distinct WPs with opposite chiralities, each exhibiting twofold degeneracy and topological protection.[7] The WPs can only occur in pairs, and are connected by a topologically protected Fermi arc, which is a significant hallmark of Weyl semimetals.[8–11]

There are two types of Weyl semimetals, classified as type-I and type-II, based on the orientation of their band crossings in momentum space.[12] Type-I Weyl semimetals feature a conventional Weyl cone and respect Lorentz invariance, whereas type-II Weyl semimetals exhibit a tilted Weyl cone and break Lorentz invariance. For type-II Weyl semimetal, its low-energy excitation has no corresponding Weyl fermions in high-energy physics.[12] Candidates for type-II Weyl semimetals have been predicted to exist in certain orthorhombic transition-metal dichalcogenides MX_2 (M = Mo, W; X = Te, P) and ternary tellurides $MM'Te_4$ (M = Ta, Nb; M' = Ir, Rh).[13–18]

Certain materials, such as noncentrosymmetric polar hexagonal (SrHgPb), noncentrosymmetric transition metal monochalcogenides (MoTe, WTe), half-Heusler compound (LaPtBi), have been proposed as candidates capable of hosting unique coexistence of Dirac and Weyl phases.[19–21] Normally, the coexistence of Dirac points and Weyl points within the same material is a rare and intriguing phenomenon due to their contrasting symmetry requirements.[5–7] Thus, the simultaneous existence of DPs, type-I, and type-II WPs in a single system has attracted researchers' interest. Recently, $NbIrTe_4$ was considered a type-II Weyl semimetal with 8 pairs of WPs.[17,22,23] However, the controversy was raised that only 4 type-II WPs exist in this material.[24] This controversy needs to be cleared. In addition, possible existence of DPs in this ternary tellurides deserves detailed study.

In this paper, combing angle-resolved photoemission spectroscopy (ARPES) measurement and density functional

[†]These authors contributed equally to this work.
[‡]Corresponding author. E-mail: guopengjie@ruc.edu.cn
[§]Corresponding author. E-mail: hlei@ruc.edu.cn
[¶]Corresponding author. E-mail: scw@ruc.edu.cn

© 2024 Chinese Physical Society and IOP Publishing Ltd

theory (DFT) calculations, we explore the electronic structures and topological properties of $NbIrTe_4$. From the DFT calculation, $NbIrTe_4$ presents 8 pairs of Weyl points. They separate from each other well in momentum space, facilitating their distinguishability. In Weyl semimetals, the Fermi arcs on the up and bottom surfaces have different connection paths and form an inter-surface Fermi arc loop. By examining the constant energy contours on surfaces, we trace the Fermi arcs' evolution and identify their ending points (source and sink of the Weyl pairs). Furthermore, through DFT calculation, there exist several DPs at $k_z = \pi$ plane, which are protected by nonsymmorphic symmetry. From the ARPES spectra, we present compelling evidence for the existence of Fermi arcs and several DPs along high-symmetry paths in $NbIrTe_4$, substantiating its classification as a topological semimetal that intriguingly accommodates both Dirac and Weyl fermions. $NbIrTe_4$ exhibits fascinating topological properties coupled with weak interlayer interaction, making it an ideal platform for further investigations of the interplay between coexisting Dirac fermions and Weyl fermions within a single material. This discovery not only enhances our understanding of quantum materials but also provides a fertile ground for future studies into the practical applications of these unique electronic properties.

2. Methods

$NbIrTe_4$ single crystals were grown by flux method. Nb powder, Ir powder and Te lump were weighed with the ratio of Nb : Ir : Te = 1 : 1 : 20. The mixture was loaded into a corundum crucible sealed into a quartz tube. The tube was then placed into a furnace, slowly heated to 1000 °C and held there for 20 h to allow sufficient homogenization. After a slow cooling to 650 °C at a rate of 2 °C/h, the single crystals were obtained after centrifuging.

High-resolution ARPES measurements were performed at the 03U beamline at the SSRF (Shanghai, China) using photon energies ranging from 20 eV to 100 eV. The samples were cleaved *in situ* with a vacuum better than 6.3×10^{-11} Torr at base temperature. The samples were measured at temperature of $T = 30$ K. The structure characterization of $NbIrTe_4$ was performed by refined x-ray diffraction (XRD) at room temperature.

First-principles electronic structure calculations were performed with the projector-augmented wave (PAW) method[25,26] as implemented in the Vienna *ab initio* simulation package (VASP).[27–29] The generalized gradient approximation (GGA) of the Perdew–Burke–Ernerh (PBE) type[30] was adopted for the exchange–correlation potential. The kinetic energy cutoff point for the plane wave basis was set to be 400 eV. For the Brillouin zone sampling, a $18 \times 6 \times 6$ k-point mesh was employed. Gaussian smearing with a width of 0.01 eV was used around the Fermi surface. In structural optimization, both cell parameters and internal atomic positions were allowed to relax until all forces on the atoms were smaller than 0.01 eV/Å. The relaxed structure parameters are well agreed with the experimental results. The spin–orbital-coupling (SOC) effect was included in the calculations of the electronic properties. The topological properties were calculated by using the wannier90 package[31,32] and WannierTools[33] package.

3. Results and discussion

$NbIrTe_4$ possesses a noncentrosymmetric orthorhombic crystal structure and is stacked along c axis, as illustrated in Fig. 1(a), with the space group $Pmn2_1$. The alternating Nb and Ir atoms form quasi-one-dimensional zigzag chains along the a-axis, and these chains are repeated in the pattern [—Ir–Nb—Nb–Ir—] along the b-axis. The unique positioning of Nb atoms, encased within three atomic layers, guarantees the robust Z_2 topology of the system.[18]

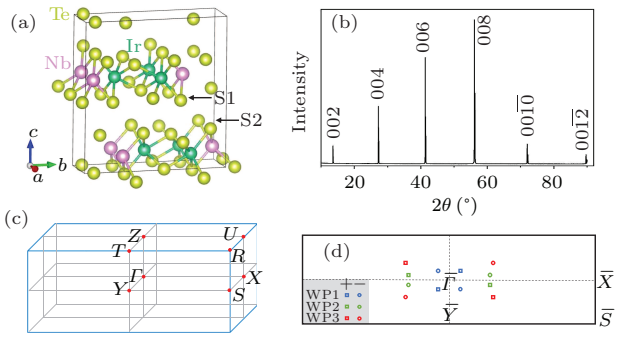


Fig. 1. (a) Crystal structure of $NbIrTe_4$. The pink, yellow and green balls are Nb, Ir and Te atoms, respectively. (b) XRD of $NbIrTe_4$ single crystal. (c) The three-dimensional Brillouin zone (BZ) of $NbIrTe_4$ with high-symmetry points. (d) Schematic of the proposed Weyl points with chiralities on projected (001) 2D BZ.

Within a unit cell, the crystal structure features two reflection symmetries: a mirror plane on the yz plane and a glide plane which combines reflection and translation across the xz plane. This glide symmetry results in two distinct exposed surfaces upon cleavage, referred to as S1 and S2 [Fig. 1(a)]. The single-crystal XRD pattern of $NbIrTe_4$, depicted in Fig. 1(b), showcases sharp peaks, indicative of high-quality crystal formation. These peaks can be indexed as (0 0 2l), confirming that the crystallographic c-axis aligns perpendicular to the crystal surface.

Figure 1(c) illustrates the first Brillouin zone (BZ) of $NbIrTe_4$, highlighting its high-symmetry points. The time-reversal invariant nature of $NbIrTe_4$ allows for the existence of various WPs within the BZ. Based on our DFT calculations, these WPs are presented on the (001) surface projection, as shown in Fig. 1(d). Detailed information about these points is provided in Table 1. Among the 16 identified points, WP1 and WP2 are classified as type-II WPs, while WP3 is categorized

under type-I. The spatial separation of these points in momentum space facilitates their distinguishability. Table 1 indicates that WP2 and WP3 are located above the Fermi level (E_F), while WP1 lies below E_F, making WP1 the only detectable Weyl point via ARPES in $NbIrTe_4$. Nonetheless, the surface states associated with WP2 and WP3 extend below E_F and become also observable in our study, which will be discussed later in detail.

Table 1. The position, chirality, and energy of the Weyl points.

Weyl points	Position ($\frac{2\pi}{a}$, $\frac{2\pi}{b}$, $\frac{2\pi}{c}$)	C	E (meV)
WP1	(0.037, 0.093, 0.178)	−1	−85
WP2	(0.137, 0.046, 0.0)	+1	117.6
WP3	(0.146, 0.179, 0.0)	+1	127

We took the high-resolution ARPES measurements on both S1 and S2 terminations of $NbIrTe_4$ and show the results in Figs. 2 and 3, respectively. On the Fermi surface intensity plot of S1 termination, as shown in Fig. 2(a), several features are observed, i.e., two elliptical-shaped features circled around $\overline{Y}$ point, an eight-curve shape surrounding $\overline{\Gamma}$ point, and two hemisphere-shaped blobs. On another termination (S2), as depicted in Fig. 3(a), the Fermi surface intensity plot is qualitatively different from that on termination S1, i.e., two nearly parallel line-shaped Fermi surfaces on both sides of $\overline{\Gamma}$ along k_y direction and two arc-like features along $\overline{Y}$–$\overline{S}$ direction, except the hemisphere-shaped blobs.

Then we plot the 2D intensity plots along high symmetry directions ($\overline{\Gamma}$–$\overline{X}$, $\overline{\Gamma}$–$\overline{Y}$, $\overline{Y}$–$\overline{S}$) for both terminations, where the clear band dispersions corresponding to Fermi surfaces are shown [Figs. 2(b) and 3(b)]. Along $\overline{\Gamma}$–$\overline{X}$, two electron-like bands with weak intensities are observable around $\overline{\Gamma}$ on S1 termination. On S2 termination, two electron-like bands are seen, but with slightly different crossing position (k_F). The most salient difference is the enhanced intensity of the hole-like band which forms the parallel-shaped FS (indicated by the orange arrows) shown in Fig. 3(a). Along the $\overline{\Gamma}$–$\overline{Y}$ direction, around $\overline{Y}$ point on S1 termination [Fig. 2(b)], one band with high intensity and one with weaker intensity are seen and across E_F at nearly the same $k_F \sim 0.2$ Å. At the S2 termination [Fig. 3(b)], these bands become flattened, and no band crossing at E_F can be observed. Along the $\overline{Y}$–$\overline{S}$ direction, around $\overline{Y}$ point on S1 termination [Fig. 2(b)], two hole-like bands with extrapolated crossing points above E_F are seen. At the S2 termination [Fig. 2(b)], the two electron-like bands across E_F, in great contrast to the hole-like bands seen on the S1 termination.

To distinguish between surface and bulk contributions, calculations were performed for both terminations. The calculated Fermi surfaces and the band dispersion along three high-symmetry lines, which correspond to their ARPES observations, are shown in Figs. 2(c)–2(d) and 3(c)–3(d), respectively. The alignment of the ARPES spectra with the DFT calculations is quantitatively well, after a 35 meV downshift of the Fermi level, indicating a close correspondence between the experimental data and theoretical predictions. This comparison enables us to differentiate between surface states (SS) and bulk states (BS), as labeled in Figs. 2 and 3. From the figures, we find out that the electron states near E_F are predominantly from surface states. One feature that can be observed on both terminations is the limited intensity with slightly enhanced edges located between $\overline{\Gamma}$–$\overline{X}$. This feature is attributed to the projection of bulk states, and is observed as the blobs in ARPES data on both S1 and S2 terminations.

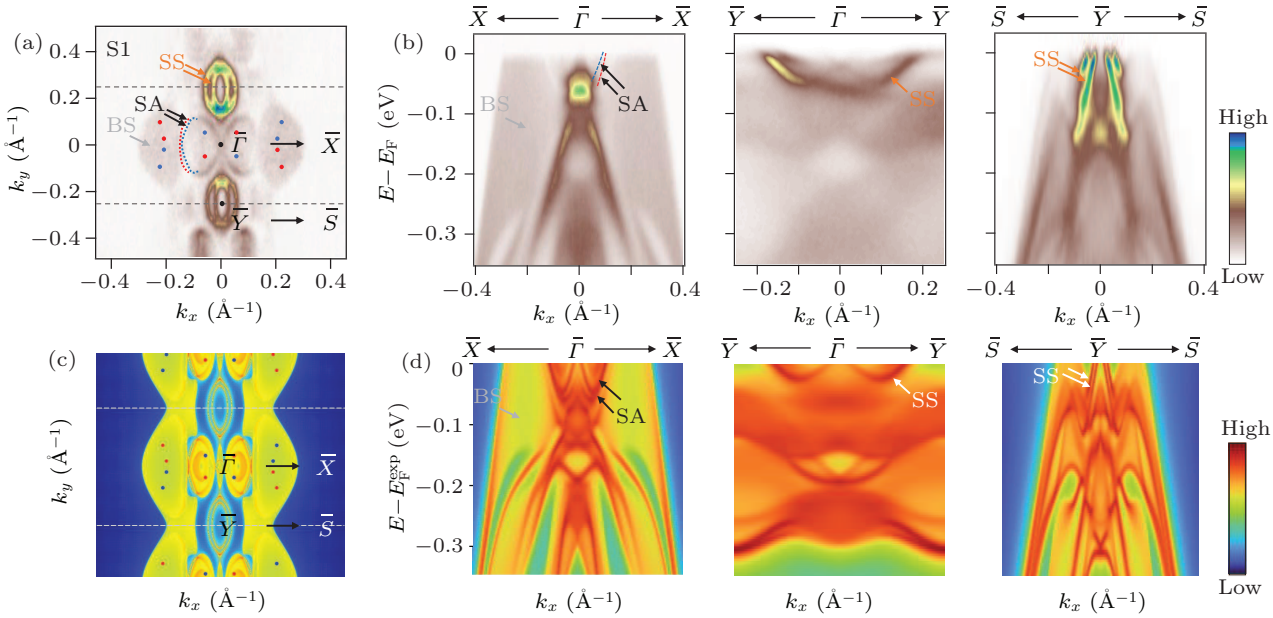


Fig. 2. ARPES measurements and DFT calculations of $NbIrTe_4$ on the S1 termination. (a) Integrated intensity map within $E_F \pm 20$ meV of ARPES measurement. The blue and red dots are the calculated Weyl points with chiralities of −1 and +1, respectively. (b) Intensity plot by APRES along high symmetry directions $\overline{\Gamma}$–$\overline{X}$, $\overline{\Gamma}$–$\overline{Y}$ and $\overline{S}$–$\overline{Y}$, respectively. (c) Spectral function of $NbIrTe_4$. The blue and red dots are the calculated Weyl points with chiralities of −1 and +1, respectively. (d) Calculated electronic structure along high symmetry directions corresponding to that in (b). The SS and SA stand for (trivial) surface state and (nontrivial) surface arc, respectively.

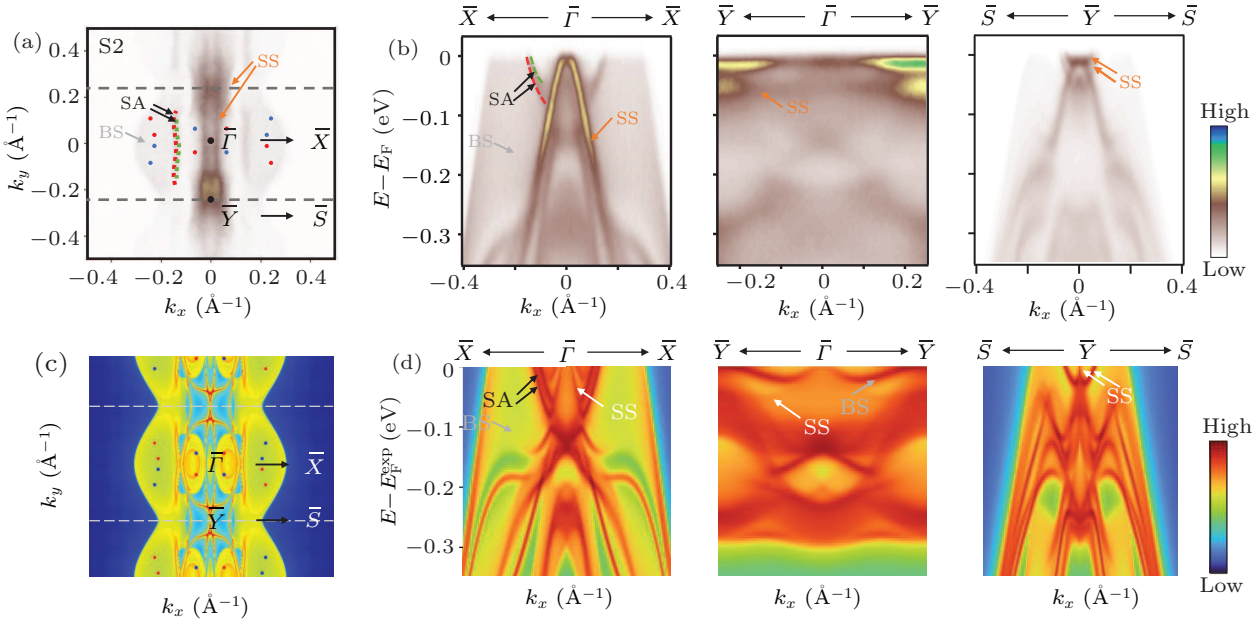


Fig. 3. ARPES measurements and DFT calculations of $NbIrTe_4$ on the S2 termination. (a) Integrated intensity map within $E_F \pm 20$ meV of ARPES measurement. The blue and red dots are the calculated Weyl points with chiralities of -1 and $+1$, respectively. (b) Intensity plot by APRES along high symmetry directions $\bar{\Gamma}$–$\bar{X}$, $\bar{\Gamma}$–$\bar{Y}$ and $\bar{S}$–$\bar{Y}$, respectively. (c) Spectral function of $NbIrTe_4$. The blue and red dots are the calculated Weyl points with chiralities of -1 and $+1$, respectively. (d) Calculated electronic structure along high symmetry directions corresponding to that in (b). The SS an SA stand for (trivial) surface state and (nontrivial) surface arc, respectively.

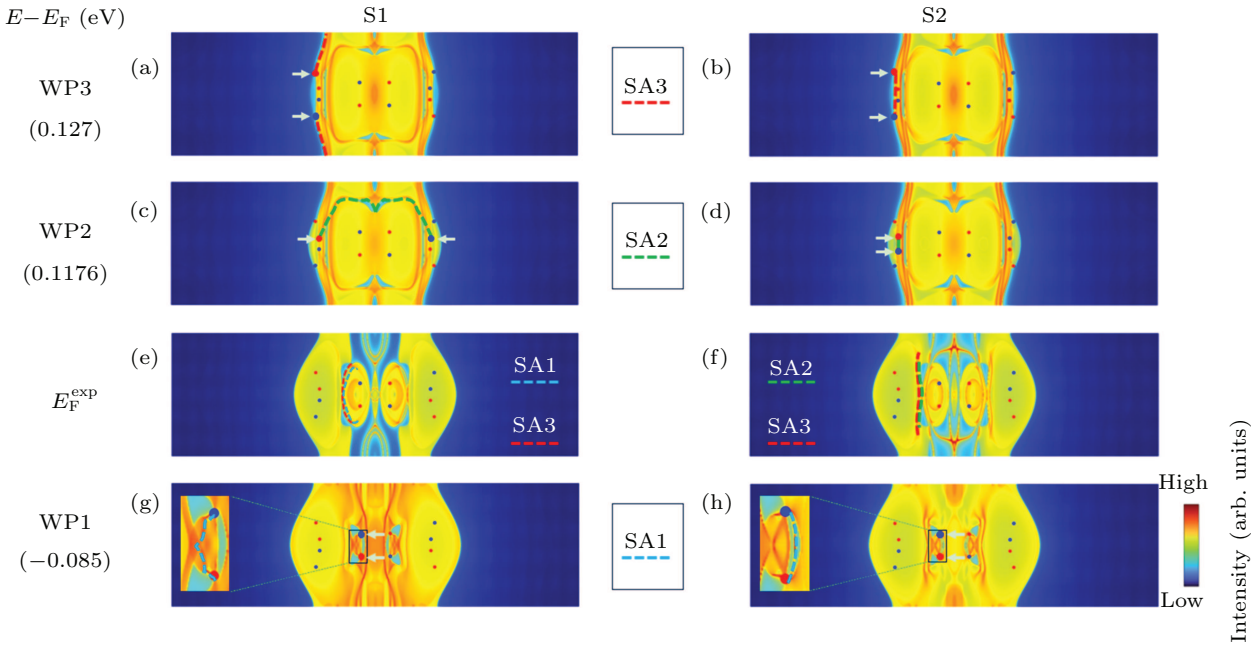


Fig. 4. Spectral functions at various energies on both terminations of $NbIrTe_4$. (a), (c) and (g) Calculated spectral function intensities on S1 termination at the energies corresponding to Weyl points W1, W2 and W3, respectively. (b), (d) and (h) Calculated spectral function intensities on S2 termination at the energies corresponding to Weyl points W1, W2 and W3, respectively. (e) and (f) Calculated spectral function intensities on S1 and S2 terminations, respectively, at the experimental Fermi level E_F^{exp}. The insets in (g) and (h) are the zoomed-in part of the dashed box in the plot. The dotted lines with different colors represent the Fermi arcs (SA3 red, SA2 green, SA1 blue). The corresponding Weyl points are indicated by the white arrows.

The existence of Fermi arcs that connect the Weyl points with opposite chiralities, which are the characteristic features apart from the linear band dispersion near E_F in Weyl semimetals, is further explored in our study. Figure 4 presents the calculated Fermi arcs at different energy levels corresponding to various WPs. The arcs on the S1 and S2 terminations show different connections and formations. For the WP3, which is located at 0.127 eV above E_F, the arc at S1 termination (SA3) connects WPs with opposite chirality from different BZs [Fig. 4(a)], and the arc at S2 termination connects the WPs within the same first BZ [Fig. 4(b)]. The arcs of WP3 on S1 and S2 would form a Fermi loop which displays as an open line along the k_y direction. For the WP2 (WP1) which is located at 0.118 eV above (0.085 eV below) E_F, the arcs (SA2

and SA1) at both terminations connect Weyl points within the same BZ [Figs. 4(c), 4(d), 4(g) and 4(h)]. The arcs on S1 and S2 form closed loops referred to as Weyl orbits at their corresponding energies.[34–36] By comparing the constant energy plots from the calculation, we trace the evolution of the surface arcs and assign the observed arcs at E_F from ARPES measurements to the corresponding WPs. At the experimental Fermi level (E_F^{exp}), we observe Fermi arcs arising from surface states associated with WP1/WP3 as SA1/SA3 on the S1 termination [Fig. 4(e)] and from the states with WP2/WP3 as SA2/SA3 on the S2 termination [Fig. 4(f)]. The Fermi surface topologies from these calculations align well with ARPES measurements. From the above correspondence between theory and ARPES experiments, we summarize the information in Figs. 2(a) and 3(a) for both terminations, where the SAs, trivial SSs, and BSs are marked in the experimental intensity plots.

Weyl points typically exist due to either inversion or time-reversal symmetry breaking of the crystal, which often precludes the presence of DPs. However, through a combination of DFT calculations and ARPES measurements, several DPs located at the high-symmetry plane ($k_z = \pi$) are confirmed, despite their broken inversion symmetry. As depicted in Fig. 5(d), these DPs are situated at the high symmetry points Z and T, where they are protected by the nonsymmorphic symmetry. To analyze the band dispersion around the Z or T points on the $k_z = \pi$ plane, we performed a photon energy-dependent measurement ranging from 20 eV to 100 eV, which covers multiple BZs along c-axis [Fig. 5(a)]. We generated the 2D intensity plot along the U–Z–U direction at $k_z = \pi$ plane and present it in Fig. 5(b). Albeit the complex nature of the band structure where DPs intersect with other BSs and other trivial SSs, the intensity plot reveals several linear dispersions with crossing energies between 0.3–1.2 eV below E_F. Then we take the 2D curvature intensity plot of Fig. 5(b) to enhance the band dispersions and the crossing points, the result is shown in Fig. 5(c). From Figs. 5(b) and 5(c), we identify four linear band crossings, labeled as α, β, γ, and δ, demarcated with brown dotted lines. The energies of these crossings are in good consistency with the theoretically predicted energies of the Dirac points.

Our research conclusively demonstrates that $NbIrTe_4$ is an exceptional topological semimetal, uniquely characterized by the coexistence of Weyl and Dirac points. This coexistence challenges the traditional understanding of symmetry requirements in topological materials, as Dirac and Weyl semimetals typically require paradoxical symmetries. Previous investigations have identified only a limited number of potential candidates capable of realizing this intriguing coexistence. For instance, in the half-Heusler compound LaPtBi, the coexistence of WPs and DPs was proposed to be induced under compressive strain.[19] In noncentrosymmetric transition metal monochalcogenides MoTe and WTe, Dirac points and type-I WPs were also proposed to be stabilized by a threefold rotational symmetry.[21] In $NbIrTe_4$, which has a noncentrosymmetric orthorhombic crystal structure, the high-symmetry Z (0, 0, π) and T (0, π, π) points exhibit specific symmetries, including C_z (1/2, 0, 1/2), M_y, M_x (1/2, 0, 1/2), T, TC_z (1/2, 0, 1/2), TM_y and TM_x (1/2, 0, 1/2). Considering the fractional translation along the z direction, we can assume that the Bloch wave function $\Psi(k)$ is an eigenstate of C_z (1/2, 0, 1/2) with eigenvalue 1, where k represents the high-symmetry Z and T points. Since both the Z and T points are time-reversal invariant points, $\Psi(k)$ and $T\Psi(k)$ form a pair of Kramers degenerate states. And $T\Psi(k)$ is also an eigenstate of C_z (1/2, 0, 1/2) with eigenvalue 1. On the other hand, due to the anti-commutation of C_z (1/2, 0, 1/2) and M_y with spin–orbit coupling, both $M_y\Psi(k)$ and $M_yT\Psi(k)$ are eigenstates of C_z (1/2, 0, 1/2) with eigenvalue -1. Meanwhile, the Bloch Hamiltonian commutes with C_z (1/2, 0, 1/2), M_y, M_x (1/2, 0, 1/2) and T, which results in a fourfold degeneracy of these four states ($\Psi(k)$, $T\Psi(k)$, $M_y\Psi(k)$, $M_yT\Psi(k)$) at the high-symmetry Z and T points. This analysis confirms that $NbIrTe_4$ is also a Dirac semimetal, characterized by its protection under nonsymmorphic symmetry.

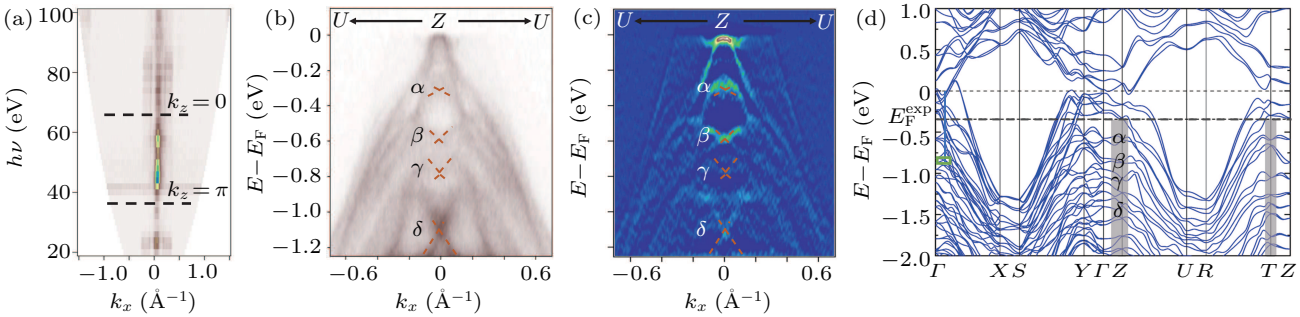


Fig. 5. Dirac points in $NbIrTe_4$ (a) Intensity of k_x–k_z plane by photon energy dependent measurement ranging from $h\nu = 20$ eV to 100 eV. (b) ARPES 2D intensity plot at $k_z = \pi$ along high symmetry directions U–Z–U. (c) 2D curvature intensity plot of (b). (d) Calculated bulk band dispersion of $NbIrTe_4$. The $k_z = 0$ and $k_z = \pi$ planes are marked in (a). The Dirac crossings are marked by dotted brown lines in (b) and (c), and the shaded area in (d) highlights the calculated Dirac points.

4. Conclusion

In conclusion, through a combined approach using ARPES and DFT calculations, we have thoroughly investigated the topological properties of the noncentrosymmetric orthorhombic crystal $NbIrTe_4$. Our study presents evidence for the presence of Weyl points within this material. By analyzing ARPES band dispersions and constant energy plots on both surface terminations, we successfully identified several Fermi arcs at each termination. Tracking the evolution of these Fermi arcs across various binding energies enabled us to attach these arcs to multiple pairs of Weyl points, with their locations and quantities aligning with prior theoretical predictions.[17,22] Furthermore, our findings substantiate the unique coexistence of Dirac and Weyl points, encompassing both type I and type II characteristics, in $NbIrTe_4$, a phenomenon intricately tied to its distinct crystal symmetry.

Acknowledgements

Project supported by the National Natural Science Foundation of China (Grant Nos. 12274455, 12274459, and 12204533), the National Key R&D Program of China (Grant No. 2022YFA1403800), and the Beijing Natural Science Foundation (Grant No. Z200005).

References

[1] Nielsen H B and Ninomiya M 1983 *Phys. Rev. B* **130** 389
[2] Shekhar C, Nayak A K, Sun Y, Schmidt M, Nicklas M, Leermakers I, Zeitler U, Skourski Y, Wosnitza J, Liu Z, *et al.* 2015 *Nat. Phys.* **11** 645
[3] Huang X, Zhao L, Long Y, Wang P, Chen D, Yang Z, Liang H, Xue M, Weng H, Fang Z, *et al.* 2015 *Phys. Rev. X* **5** 031023
[4] Gorbar E, Miransky V and Shovkovy I 2014 *Phys. Rev. B* **89** 085126
[5] Armitage N, Mele E and Vishwanath A 2018 *Rev. Mod. Phys.* **90** 015001
[6] Hasan M Z, Xu S Y, Belopolski I and Huang S M 2017 *Annu. Rev. Condens. Matter Phys.* **8** 289
[7] Vafek O and Vishwanath A 2014 *Annu. Rev. Condens. Matter Phys.* **5** 83
[8] Young S M, Zaheer S, Teo J C, Kane C L, Mele E J and Rappe A M 2012 *Phys. Rev. Lett.* **108** 140405
[9] Wan X, Turner A M, Vishwanath A and Savrasov S Y 2011 *Phys. Rev. B* **83** 205101
[10] Burkov A and Balents L 2011 *Phys. Rev. Lett.* **107** 127205
[11] Witczak-Krempa W and Kim Y B 2012 *Phys. Rev. B* **85** 045124
[12] Soluyanov A A, Gresch D, Wang Z, Wu Q, Troyer M, Dai X and Bernevig B A 2015 *Nature* **527** 495
[13] Sun Y, Wu S C, Ali M N, Felser C and Yan B 2015 *Phys. Rev. B* **92** 161107
[14] Wang Z, Gresch D, Soluyanov A A, Xie W, Kushwaha S, Dai X, Troyer M, Cava R J and Bernevig B A 2016 *Phys. Rev. Lett.* **117** 056805
[15] Autes G, Gresch D, Troyer M, Soluyanov A A and Yazyev O V 2016 *Phys. Rev. Lett.* **117** 066402
[16] Koepernik K, Kasinathan D, Efremov D, Khim S, Borisenko S, Büchner B and van den Brink J 2016 *Phys. Rev. B* **93** 201101
[17] Li L, Xie H H, Zhao J S, Liu X X, Deng J B, Hu X R and Tao X M 2017 *Phys. Rev. B* **96** 024106
[18] Liu J, Wang H, Fang C, Fu L and Qian X 2017 *Nano Lett.* **17** 467
[19] Lau A, Koepernik K, van den Brink J and Ortix C 2017 *Phys. Rev. Lett.* **119** 076801
[20] Gao H, Kim Y, Venderbos J W, Kane C, Mele E, Rappe A M and Ren W 2018 *Phys. Rev. Lett.* **121** 106404
[21] Meng L, Wu J, Li Y and Zhong J 2019 *J. Mater. Chem. C* **7** 12151
[22] Wang Z, Huang C Y, Hsu C H, Namiki H, Chang T R, Chuang F C, Lin H, Sasagawa T, Madhavan V and Okada Y 2022 *Phys. Rev. B* **105** 075110
[23] Huang X W, Liu X X, Yu P, Li P L, Cui J, Yi J, Deng J B, Fan J, Ji Z Q, Qu F M, *et al.* 2019 *Chin. Phys. Lett.* **36** 077101
[24] Ekahana S A, Li Y W, Sun Y, Namiki H, Yang H F, Jiang J, Yang L X, Shi W J, Zhang C F, Pei D, Chen C, Sasagawa T, Felser C, Yan B H, Liu Z K and Chen Y L 2020 *Phys. Rev. B* **102** 085126
[25] Blöchl P E 1994 *Phys. Rev. B* **50** 17953
[26] Kresse G and Joubert D 1999 *Phys. Rev. B* **59** 1758
[27] Kresse G and Hafner J 1993 *Phys. Rev. B* **47** 558
[28] Kresse G and Furthmüller J 1996 *Comp. Mater. Sci.* **6** 15
[29] Kresse G and Furthmüller J 1996 *Phys. Rev. B* **54** 11169
[30] Perdew J P, Burke K and Ernzerhof M 1996 *Phys. Rev. Lett.* **77** 3865
[31] Souza I, Marzari N and Vanderbilt D 2001 *Phys. Rev. B* **65** 035109
[32] Marzari N and Vanderbilt D 1997 *Phys. Rev. B* **56** 12847
[33] Wu Q, Zhang S, Song H F, Troyer M and Soluyanov A A 2018 *Computer Physics Communications* **224** 405
[34] Potter A C, Kimchi I and Vishwanath A 2014 *Nat. Commun.* **5** 5161
[35] Bulmash D and Qi X L 2016 *Phys. Rev. B* **93** 081103
[36] Moll P J, Nair N L, Helm T, Potter A C, Kimchi I, Vishwanath A and Analytis J G 2016 *Nature* **535** 266